Mapping and Understanding the Synergy Between Land Surface Temperature and $PM_{2.5}$ at 250 m Resolution in Wuhan: Implications for Climate Adaptation and Air Quality Management

Ruihan Qiu [12], Qingming Zhan[12*], Shiqi Tu [12], Changling Li[12], Yilei Zhang [12]

[1] School of Urban Design, Wuhan University, Wuhan 430072, China
[2] Research Centre for Digital City, Wuhan University,Wuhan 430072, China

* Corresponding author: qmzhan@whu.edu.cn

Keywords: Land Surface Temperature, $PM_{2.5}$, Downscaling, Synergy analysis, Remote sensing, Wuhan

ABSTRACT

Urban $PM_{2.5}$ pollution and land surface temperature (LST) are key indicators of urban environmental quality, yet their fine-scale coupling over decadal periods is still unclear. This study maps $PM_{2.5}$ at 250 m resolution in central Wuhan, China, for 2015, 2020 and 2025, using summer, winter and annual composites. A three-stage downscaling framework was developed. First, multi-source predictors, including satellite $PM_{2.5}$, MODIS products, ERA5 meteorology, topography, population and road data, were screened by Variance Inflation Factor analysis, reducing 24 variables to 18. Second, Random Forest, XGBoost and LightGBM were trained on nine year–season datasets. Random Forest performed best in all cases, with test-set R^2 ranging from 0.531 to 0.936 and near-zero bias ($|Bias| \leq 0.10$ μg/m³). Third, the 1 km RF models were applied to 250 m grids, with station-based IDW residual correction where bias exceeded 1 μg/m³. Leave-One-Out Cross-Validation showed an average RMSE reduction of about 35%.

The results show that annual mean $PM_{2.5}$ decreased by 47.5% from 2015 to 2025 (69.28 to 36.39 μg m^{-3}), while summer LST increased by 1.39°C. This “cleaner but hotter” pattern indicates a weakening of aerosol-related cooling as $PM_{2.5}$ declined. Pearson correlation analysis at 250 m and 1 km shows that the LST–$PM_{2.5}$ relationship shifted from weak or negative in 2015 to positive by 2025, with annual r_{250m} reaching 0.335. The highest $PM_{2.5}$ quintile showed the strongest coupling, reaching r = 0.51 in 2025. These findings support coordinated air-quality and heat-risk management.

1. Introduction

Urban air quality degradation and intensifying thermal environments have emerged as two defining environmental challenges confronting sustainable urban development worldwide (Akbari, Pomerantz, and Taha 2001; Ngarambe et al., 2021).

Their consequences for public health, energy systems, and socioeconomic wellbeing are well established yet persistently severe: prolonged exposure to fine particulate matter ($PM_{2.5}$) elevates the risk of cardiopulmonary disease and premature mortality(Cohen et al., 2017), while the compounding effects of heat waves and the urban heat island (UHI) phenomenon significantly increase heat-related mortality and peak energy demand (Giridharan and Emmanuel 2018; Kouis et al., 2019).

In China, concerted emission-control efforts have produced measurable progress since the State Council issued the Air Pollution Prevention and Control Action Plan in 2013, which reduced annual mean $PM_{2.5}$ concentrations in the Beijing–Tianjin–Hebei, Yangtze River Delta, and Pearl River Delta regions by 39.6%, 34.3%, and 27.7%, respectively, relative to 2013 baselines (Wu et al., 2024). Subsequent policy documents — the Three-Year Action Plan for Clean Air (2018) and the Action Plan for Continuous Improvement of Air Quality (2023) — have sustained this trajectory. Nonetheless, the national urban $PM_{2.5}$ annual mean stood at 29.3 μg/m³ in 2024, substantially exceeding the updated World Health Organization (WHO) annual guideline of 5 μg/m³ (Lin et al., 2025). In the study area of Wuhan, the central urban zone recorded an annual mean of 30.68 μg/m³ in 2025 — marginally below the Chinese national standard 35μg/m³ yet still more than six times the WHO target — underscoring that the health burden from $PM_{2.5}$ exposure remains substantial even in a decade of documented improvement.

Concurrent with these air quality changes, rapid urbanisation has fundamentally altered the urban land surface. The large-scale conversion of natural and semi-natural cover to impervious surfaces, combined with intensifying anthropogenic heat release and long-term climate warming, has driven progressive strengthening of the UHI effect(Oke 1982; Wong et al., 2021).

Within the heterogeneous built environment, variations in urban morphology and functional land use modify the surface energy balance, local ventilation, and anthropogenic heat fluxes, generating pronounced spatial differentiation in the thermal environment (Guo et al., 2015; Shao et al., 2023). Certain districts thus emerge as persistent thermal hotspots — areas where summer heat stress compounds UHI risks and winter pollution episodes create co-occurring respiratory hazards (Cao et al., 2024; Xin Chen and Wei 2025; Zhe Wang et al., 2020).

Importantly, these thermal and pollution pressures do not evolve independently: as emission controls progressively reduce $PM_{2.5}$ burdens, the relative importance of urban structural factors in governing both pollutant dispersion and surface heat loading is expected to grow, yet the pace and nature of this structural shift remain poorly characterised. Despite their simultaneous occurrence and shared urban drivers, $PM_{2.5}$ and land surface temperature (LST) have largely been investigated as independent phenomena. Existing literature on $PM_{2.5}$ mapping predominantly exploits satellite aerosol optical depth (AOD) retrievals combined with statistical or machine learning models to generate gridded concentration products (Geng et al., 2021).

While operationally valuable, mainstream products such as TAP and ChinaHighPM25 operate at spatial resolutions of 1 km or coarser, insufficient to resolve the intra-urban heterogeneity driven by individual industrial facilities, traffic corridors, and green-space networks. Machine learning downscaling approaches have demonstrated capacity to improve spatial resolution (Jike Chen et al., 2021; Xiao et al., 2022), yet most existing implementations are limited to single time-points or short time windows, precluding systematic analysis of structural changes in $PM_{2.5}$ spatial patterns across a decade of sustained emission reduction. Meanwhile, studies of urban thermal environment evolution, although extensive, commonly suffer from temporal shallowness — analysing a single epoch or a short interval — making it difficult to characterise how LST spatial patterns restructure as co-occurring $PM_{2.5}$ regimes shift from heavily polluted to near-compliance conditions.

The coupling relationship between $PM_{2.5}$ and LST adds a further layer of complexity that the existing literature has only partially addressed. Two mechanistic pathways are now recognised. Under high $PM_{2.5}$ loading, aerosol particles scatter and absorb incoming shortwave radiation (direct radiative forcing), reducing surface-reaching solar flux and suppressing LST in heavily polluted zones, yielding a negative spatial association between $PM_{2.5}$ and LST — the aerosol radiative cooling pathway (Xiaoling Wang et al., 2023; Yang Chen et al., 2024).

As concentrations decline to moderate-to-low levels, this radiative masking weakens and LST spatial patterns become dominated by land-surface characteristics: impervious-surface-dense areas exhibit both elevated LST (high heat capacity, low albedo) and elevated $PM_{2.5}$ (poor ventilation, concentrated emissions), while vegetated zones show co-occurring low LST and low $PM_{2.5}$ via evapotranspiration-driven cooling and particle deposition — the urban morphology co-driving pathway, which produces a positive association (Li et al., 2023; Peng Cui et al., 2022).

Crucially, these two pathways have been theorised and observed individually in cross-sectional studies, but no study has yet documented the complete decadal trajectory of this coupling evolution within a single urban spatial framework spanning the transition from high-pollution to near-compliance conditions.

Three critical gaps therefore motivate the present study. First, existing urban $PM_{2.5}$ mapping remains at 1 km resolution, inadequate for resolving the sub-kilometre spatial heterogeneity that characterises dense Chinese megacities. Second, no analysis has spanned the full 2015–2025 window capturing the transition from high-pollution to near-compliance conditions, preventing observation of how LST–$PM_{2.5}$ coupling evolves across the complete policy-driven concentration decline. Third, while the two mechanistic pathways are conceptually established, the intra-annual concentration-stratified structure of their co-existence — and how that structure shifts as decadal reduction unfolds — has not been empirically characterised at fine spatial resolution.

This study addresses all three gaps through a unified framework applied to the central urban area of Wuhan, China (2015, 2020, 2025; summer, winter, and annual composites; n = 9 datasets, ~53,000 grid cells per dataset at 250 m). The specific objectives are: (1) to develop and validate a three-stage 250 m $PM_{2.5}$ downscaling framework combining Random Forest modelling with IDW station-residual correction and spatial leave-one-out cross-validation; (2) to characterise the decadal spatiotemporal evolution of $PM_{2.5}$ and downscaled LST at 250 m resolution across nine year–season composites; and (3) to quantify the interannual trajectory of the dual-scale LST–$PM_{2.5}$ spatial coupling and examine how within-year concentration stratification reveals the co-existence and sequential dominance of aerosol radiative cooling and urban morphology co-driving mechanisms across the decade of emission reduction.

2. Study area and Data Sources

This study integrates a multi-source geospatial dataset to construct a comprehensivespatial modelling framework for downscaling $PM_{2.5}$ concentrations to 250 m resolution and for examining the spatiotemporal coupling between $PM_{2.5}$ and land surface temperature (LST) across three epochs (2015, 2020, 2025) and three seasonal composites (summer: June–August; winter: December–February; annual mean). All input datasets are organised into two functional categories: (i) the modelling target variable — gridded $PM_{2.5}$ at 1 km resolution from the Tracking Air Pollution in China (TAP) platform (Geng et al., 2021; Xiao et al., 2022), corrected at the local scale via station-based IDW residual adjustment; and (ii) predictor covariates spanning satellite remote sensing, meteorological reanalysis, urban morphology, and socioeconomic indicators. LST data were obtained from the MODIS Land Surface Temperature product (MOD11A2, Version 6.1; 1 km, 8-day composite); raw digital numbers were scaled by a factor of 0.02 and converted from Kelvin to degrees Celsius, and seasonal means were computed for the summer (June–August), winter (December–February), and annual composites. All griddedproducts were resampled to a common 1 km reference grid for model training and to a 250 m grid for the downscaled output; multicollinearity among covariates was assessed via Variance Inflation Factor (VIF) screening prior to model fitting. The full dataset inventory, including spatial and temporal resolutions, is summarised in Table 1.

Table1. Multi-source input dataset overview, including modelling target variable, remote sensing products, meteorological reanalysis, and urban morphology data used.

Data	Spatial/ Temporal Resolution	Sources	Selected Years
MODIS version6 MCD12Q1 data	500 m Monthly	https://ladsweb.modaps.eosdis.nasa.gov/search/	2015, 2020, 2025
CLCD	30m,Yearly	http://irsip.whu.edu.cn/resources/dataweb2.php	2015, 2020, 2025
NDVI	1 km	Find Data - LAADS DAAC (nasa.gov)	2015, 2020, 2025
TAP	Point	https://envidat.ch/#/metadata/bioclim_plus	2015, 2020, 2025
NOAA/VIIRS/DN	500 m	https://www.ncei.noaa.gov/maps/ VIIRS_DNB_nighttime_imagery/	2015, 2020, 2025
WorldPop	30 arcsec	https://hub.worldpop.org/	2015, 2020, 2025
OSM	Adopted 1km	https://www.openstreetmap.org/#map=8/30.534/113.939	2015, 2020, 2025

Note: For complete dataset inventory including ERA5, MODIS LST, and all predictor variables, see Table 2 below.

2.1 Study area

Wuhan, the capital of Hubei Province, China and a core node of the Yangtze River Economic Belt, is situated in central China (30.35°N–30.80°N, 113.90°E–114.60°E; Figure 1). As one of the most populous and economically dynamic megacities in inland China, Wuhan features a subtropical monsoon climate characterised by hot, humid summers and cold, relatively dry winters — a thermal and meteorological regime that creates strong seasonal contrasts in both $PM_{2.5}$ dispersion capacity and land surface heat loading. Mean summer (June–August) air temperatures regularly exceed 32°C, while winter (December–February) temperatures frequently fall below 5°C; planetary boundary layer heights also vary substantially between seasons, directly modulating pollutant accumulation and dilution capacity. The spatial domain of this study is the central development area of Wuhan, delineated by the Third Ring Road (Figure 1), covering approximately 680 km² and encompassing the city's primary commercial districts, transportation hubs, industrial zones, residential neighbourhoods, and major urban green spaces and water bodies (East Lake, South Lake,and the Yangtze–Han river confluence). This boundary captures the zone of highest intra-urban $PM_{2.5}$ and LST spatial heterogeneity and is served by all nine national ambient air quality monitoring stations used in this study. Concentrations across the domain have undergone dramatic change over the study period: the annual mean $PM_{2.5}$ declined from 68.81 μg/m³ in 2015 to 36.21 μg/m³ in 2025, while summer land surface temperature simultaneously increased from 31.02°C to 32.41°C — the divergent trajectories that motivate the core analysis of this paper. Three representative years — 2015, 2020, and 2025 — were selected to align with key milestones in China's ambient air quality governance: 2015 corresponds to the mid-implementation phase of the Air Pollution Prevention and Control Action Plan ("Atmosphere Ten"); 2020 marks the conclusion year of the Three-Year Action Plan for Clean Air and coincides with the COVID-19 lockdown period, whose anomalous emission suppression provides a natural experiment for examining $PM_{2.5}$–LST coupling under extreme low-concentration conditions; 2025 represents the most recent baseline under the Action Plan for Continuous Improvement of Air Quality. Together, the three epochs span a decade of sustained policy-driven emission reduction, enabling systematic characterisation of both long-term structural trends and interannual mechanism transitions. For each year, three seasonal composites are derived: summer (June–August), winter (December–February), and annual mean — yielding nine independent datasets. Summer and winter are modelled separately to capture the strong seasonal modulation of meteorological drivers on $PM_{2.5}$spatial distribution; the annual composite is included to characterise the integrated spatiotemporal pattern and to facilitate comparison with annual-mean LST analyses.

2.2 Data sources

A multi-source dataset integrating satellite remote sensing, meteorological reanalysis, urban morphology, and ground-based observations was assembled for the study domain (Table 2). All gridded products were resampled to a common 1 km reference grid for model training and to a 250 m grid for the downscaling output stage.

(1) TAP $PM_{2.5}$ fusion product

The modelling target variable is the 1 km monthly $PM_{2.5}$ product from the Tracking Air Pollution in China (TAP) platform (Geng et al.,2021; Xiao et al.,2022). TAP assimilates

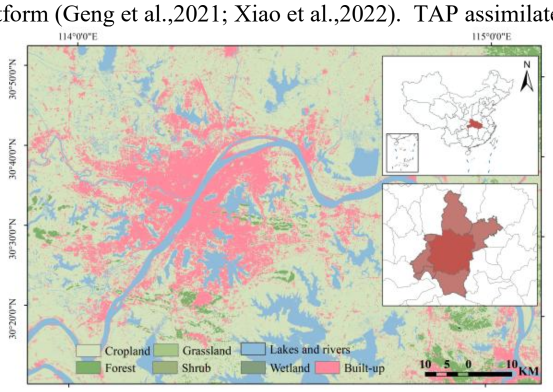

Figure 1. Study Areas in Wuhan, China

ground observations, satellite AOD retrievals, and CMAQ chemical transport model simulations through a two-stage Random Forest procedure to generate spatially complete, nationwide $PM_{2.5}$ fields. Its principal advantages over single-source satellite retrievals include full spatial coverage under cloudy conditions, superior capture of heavy-pollution episodes, and 1 km resolution sufficient to reflect intra-urban concentration gradients. However, TAP exhibits systematic biases at the local urban scale — a known limitation that directly motivates the station-residual IDW correction introduced in Stage 3 of the methodology (Section 2.3.3).

(2) ERA5 meteorological data reanalysis

Hourly atmospheric variables were extracted from the ECMWF ERA5 reanalysis at native 0.25° resolution (~28 km) and bilinearly interpolated to the 1 km study grid (Hersbachet al., 2020). Eight variables were initially retained: relative humidity (RH), 10 m windspeed (ws) and its zonal component (ws_u), planetary boundary layer height (BLP),2 m air temperature (T2m), dewpoint temperature (Td), surface pressure (SP), and total precipitation (TP). Following Variance Inflation Factor (VIF) screening (VIF < 10 threshold; Section 2.3.1), only RH, ws, ws_u, and BLP were retained for modelling; T2m, Td, SP, and TP were excluded due to multicollinearity with other predictors.

(3) MODIS remote sensing data

Three MODIS products were used. (i) MAIAC AOD (MCD19A2, 1 km, daily): derived via the Multi-Angle Implementation of Atmospheric Correction algorithm, which demonstrates superior performance over urban areas compared with standard MODIS Collection 6 AOD (Lyapustin et al.,2018). (ii) NDVI (MOD13Q1, 250 m, 16-day composite): retained at native 250 m resolution to support the spatial downscaling stage. (iii) LST (MOD11A2,1 km, 8-day composite): used both as a predictor variable in $PM_{2.5}$ modelling and as the primary response variable in the coupling analysis. All products were temporally averaged to seasonal composites; cloud-contaminated missing values were gap-filled by linear temporal interpolation.

(4) Urban morphology and social economic data

Topographic constraint on pollutant dispersion was represented by elevation from the NASA SRTM DEM (30 m), resampled to 1 km. Population density (POP_MEAN) was sourced from the WorldPop 100 m annual gridded product, aggregated to 1 km. Nighttime light intensity (NL_MEAN) from the NOAA/VIIRS monthly composites (500 m) served as a proxy for industrial production and economic activity. Road density (Road_P) was computed by kernel density estimation of OpenStreetMap road network vectors and rasterised to 1 km. Industrial point-source emission intensity (F_P) was derived analogously from the national industrial enterprise registry via kernel density analysis. Five landscape pattern metrics —PLAND, NP, SHAPE_AM, AI, and LPI — were calculated at 1 km grid scale from 30 m land-use/land-cover data (Xin Huang et al., 2021, 2022) to quantify multi-dimensional structural characteristics of the built environment.

Table 2. Multi-source modelling dataset inventory.

Dataset	Variables	Spatial Resolution	Temporal Resolution	Sources

Dataset	Variables	Spatial Resolution	Temporal Resolution	Sources
TAP $PM_{2.5}$	$PM_{2.5}$ concentration (modelling target)	1 km	Monthly	Tsinghua TAP platform
ERA5 reanalysis	RH, wind speed (ws, ws_u), BLP, T2m, Td, SP, TP	28 km (0.25°)	Hourly → seasonal mean	ECMWF
MODIS MAIAC AOD	Aerosol optical depth (MCD19A2)	1 km	Daily → seasonal mean	NASA LAADS DAAC;
MODIS NDVI	Normalised difference vegetation index (MOD13Q1)	250 m	16-day composite	NASA LAADS DAAC
MODIS LST	Land surface temperature (MOD11A2)	1 km	8-day composite	NASA LAADS DAAC
SRTM DEM	Elevation	30 m - 1 km	Static	NASA SRTM
WorldPop	Population density (POP_MEAN)	1 km (30 arcsec)	Annual	WorldPop
NPP-VIIRS NTL	Nighttime light intensity (NL_MEAN)	500 m	Monthly - seasonal mean	NOAA/ NCEI
OpenStreetMap	Road density (Road_P)	Vector- 1 km	2015, 2020, 2025	OpenStreetMap contributors
Industrial POI	Factory kernel density (F_P)	Point - 1 km KDE	2015, 2020, 2025	National enterprise registry
Landscape metrics	PLAND, NP, SHAPE_AM, AI, LPI	1 km (from 30 m LULC)	Annual	CLCD
Ground $PM_{2.5}$ stations	In-situ hourly $PM_{2.5}$	Point (9 stations)	Hourly - seasonal mean	China MEE national network

(5) Ground-based $PM_{2.5}$ monitoring stations

Hourly $PM_{2.5}$ observations from nine national ambient air quality monitoring stations operated by China's Ministry of Ecology and Environment (MEE) within the Third Ring Road boundary were aggregated to seasonal and annual means. Station-to-grid matchingused a maximum search radius of 1,500 m. The nine stations serve two roles in this study:(i) evaluation of systematic bias in the 1 km RF model relative to ground truth, and (ii) provision of residual anchor points for IDW spatial interpolation, independently validated via Leave-One-Out Cross-Validation (LOO-CV). The stations collectively represent the major functional zones of the study area — commercial core, industrialdistricts, residential neighbourhoods, and ecological green spaces — providing adequate coverage of the intra-urban $PM_{2.5}$ concentration gradient.

3. METHODOLOGY

The framework comprises three sequential stages (Figure 2): (1) multi-source feature engineering and 1 km machine learning modelling; (2) spatial downscaling to 250 m; and (3) station-based IDW residual correction with LOO-CV validation.

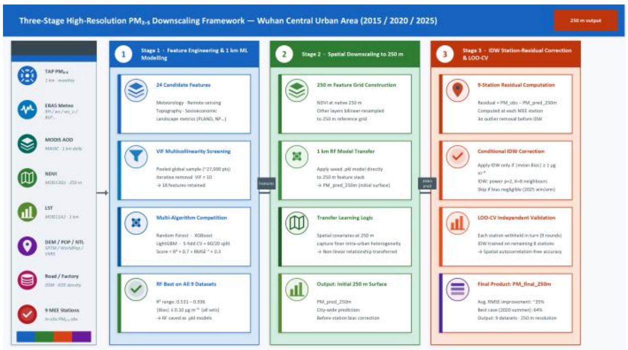

Figure 2. Three-stage 250 m $PM_{2.5}$ downscaling framework

3.1 Feature Engineering and 1 km Machine Learning Model

Twenty-four candidate predictor variables spanning meteorological, remote sensing, topographic, and socioeconomic dimensions were assembled as showed in Table 3. To eliminate multicollinearity, a global VIF screening procedure was applied: stratified random samples (~3,000 records) were drawn from each of the nine datasets and pooled (~27,000 records); predictors were iteratively removed (highest VIF first, threshold > 10) until all retained variables satisfied VIF ≤ 10 (LST retained despite marginal VIF due to its physical importance as an aerosol-radiation mediator). Eighteen predictors were retained: AOD, NDVI, LST, DEM, NL_MEAN, POP_MEAN, Road_P, F_P, Latitude, Longitude, RH, ws, ws_u, BLP, PLAND, NP, SHAPE_AM, and AI.

Three ensemble learning algorithms — Random Forest, XGBoost and LightGBM — were trained under identical conditions: fixed seed (42), 80/20 train-test split, and 5-fold cross-validation. Model selection followed a composite score ($Score = R^2 \times 0.7 + RMSE^{-1}\_normalised \times 0.3$). RF achieved the best composite score on all nine datasets and was adopted as the modelling algorithm throughout. For the two lowest-accuracy datasets (2025 summer and winter, $R^2 < 0.60$), additional hyperparameter optimisation via RandomizedSearchCV (50 iterations, 5-fold CV) was applied to RF.

3.2 Spatial Downscaling to 250 m Resolution

The trained 1 km RF model was applied directly to 250 m resolution feature grids (NDVI at native 250 m; other predictors resampled via bilinear interpolation) to generate an initial 250 m $PM_{2.5}$ prediction surface (PM_pred_250m). This transfer leverages the fact that spatial covariates at 250 m capture finer intra-urban heterogeneity, effectively transferring the learned non-linear $PM_{2.5}$–environment relationships to a higher resolution (Di et al., 2019; Jike Chen et al., 2021).

3.3 IDW Station-Residual Correction and LOO-CV

Station residuals were computed at each of the nine MEE monitoring locations (Residual = PM_obs − PM_pred_250m). Where the mean absolute bias exceeded 1 µg m⁻³, an IDW surface (power p = 2, K = 8 neighbours) was interpolated and added to PM_pred_250m to yield the corrected product PM_final_250m; otherwise PM_pred_250m was retained directly (applied to 2025 winter and annual composites). A spatial Leave-One-Out Cross-Validation (LOO-CV) — in which each station is sequentially withheld and the IDW surface trained on the remaining eight — was used to provide independent accuracy estimates (R²_LOO, RMSE_LOO, MAE_LOO), avoiding spatial autocorrelation inflation present in standard CV.

4. RESULTS AND DISCUSSION

4.1 Model Accuracy Assessment

RF achieved the best composite score on all nine datasets (Table 4). Test-set R^2 ranged from 0.531 (2025 winter) to 0.936 (2015 annual), with RMSE spanning 0.86 µg m⁻³ (2020 summer) to 4.31 µg m⁻³ (2025 winter) and near-zero systematic bias (|Bias| ≤ 0.10 µg m⁻³ across all datasets), confirming the absence of systematic overestimation or underestimation. Residual distributions were approximately normal and centred at zero for all nine datasets.

As shown in Table 4. The inter-annual accuracy decline is attributable to two factors. First, the narrowing $PM_{2.5}$ concentration range progressively reduced the signal-to-noise ratio available for model learning: the 2015 annual range (~60–78 µg m⁻³) yielded R^2 = 0.936, while the 2025 summer range (6–17 µg m⁻³) yielded R^2 = 0.607. Second, TAP product uncertainty increases in low-concentration regimes, as its estimation error constitutes a larger fraction of the total concentration range (Xiao et al., 2022). The notably higher 2025 annual R^2 (0.857) relative to seasonal composites reflects the smoothing of seasonal extremes in the annual mean.

Station-based independent validation confirmed systematic regional biases in TAP at the urban local scale (station R^2 predominantly negative; |Bias| up to 17 µg m⁻³), establishing the methodological necessity of IDW correction. LOO-CV results show an average RMSE improvement of ~35 % across the seven corrected datasets, with the best case reaching 64 % (2020 summer).

4.2 $PM_{2.5}$ Spatiotemporal Patterns (2015–2025)

Annual mean $PM_{2.5}$ declined from 69.28 µg m⁻³ (2015) to 40.89 µg m⁻³ (2020) and 36.39 µg m⁻³ (2025), a cumulative 10-year reduction of 47.5% (Figure 4; Table 5). However, the pace decelerated markedly: the 2015–2020 reduction was 28.39 µg m⁻³ (41.0%), while 2020–2025 yielded only 4.50 µg m⁻³ (11.0%), indicating that ambient $PM_{2.5}$ reduction is entering a diminishing-returns phase. Note that the 2020 values are anomalously low due to COVID-19 lockdown-induced emission suppression and should not be attributed entirely to policy-driven permanent reduction .

Table 3. Predictor variables retained after VIF screening (18 of 24 candidates; VIF threshold = 10; LST force-retained due to physical importance as aerosol–radiation mediator).

Variable	Category	Description	Source / Unit
Latitude	Spatial	Geographic latitude of grid centroid	Derived from fishnet (°N)
Longitude	Spatial	Geographic longitude of grid centroid	Derived from fishnet (°E)
AOD	Remote sensing	MAIAC aerosol optical depth at 550 nm	MODIS MCD19A2
NDVI	Remote sensing	Normalised difference vegetation index	MODIS MOD13Q1 (250 m resolution)
LST	Remote sensing	Land surface temperature (force-retained; VIF > 10)	MODIS MOD11A2 (1 km)
DEM	Topography	Elevation above sea level	NASA SRTM 30 m → 1 km (m)
NL_MEAN	Socioeconomic	Mean nighttime light intensity	NOAA/VIIRS (W·cm⁻²·sr⁻¹)
POP_MEAN	Socioeconomic	Mean population density	WorldPop 100 m (persons km⁻²)
Road_P	Socioeconomic	Road network kernel density	OpenStreetMap
F_P	Socioeconomic	Industrial facility kernel density	National enterprise registry
RH	Meteorology	Near-surface relative humidity	ERA5 reanalysis (%)
ws	Meteorology	10 m wind speed magnitude	ERA5 reanalysis (m s⁻¹)

Table 4. RF model accuracy for each of the nine datasets (test set, 1 km).

Dataset	R^2	RMSE (µg m⁻³)	MAE (µg m⁻³)	Bias (µg m⁻³)
2015 Summer	0.868	2.52	1.95	−0.06
2015 Winter	0.920	3.31	2.48	−0.01

Dataset	R^2	RMSE ($\mu g\ m^{-3}$)	MAE ($\mu g\ m^{-3}$)	Bias ($\mu g\ m^{-3}$)
2015 Annual	0.936	2.25	1.72	+0.05
2020 Summer	0.664	0.86	0.68	−0.03
2020 Winter	0.773	1.60	1.24	−0.10
2020 Annual	0.803	1.16	0.90	+0.05
2025 Summer*	0.607	1.18	0.92	−0.00
2025 Winter*	0.531	4.31	3.22	−0.07
2025 Annual	0.857	0.88	0.69	−0.01

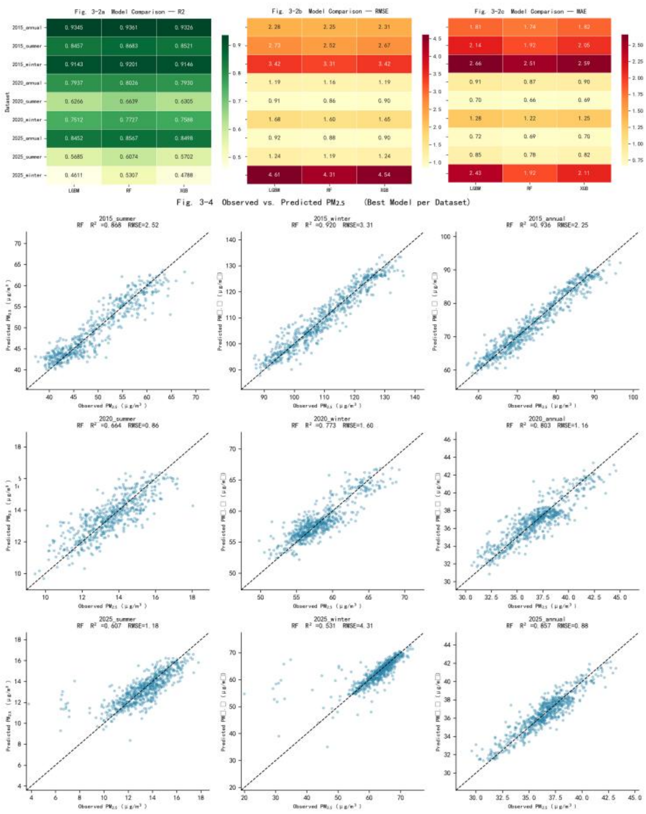

Figure 3. Multi-algorithm accuracy comparison and RF scatter plots for nine datasets.

A persistent north-high south-low spatial gradient characterised all three epochs, consistent with the dominant feature importance of Latitude (Section 4.5). However, the internal hotspot structure evolved substantially: in 2015, high-concentration zones were spatially aligned with major industrial corridors (steel and chemical plants in the Qingshan district); by 2025, residual hotspots were concentrated in logistics hubs and dense traffic nodes, reflecting a structural transition from industrial-source-dominated to traffic-and-anthropogenic-activity-dominated pollution (Figure 4).

Seasonally, the winter-to-summer concentration ratio expanded from 2.92 (2015) to 4.86 (2025), driven by dramatically asymmetric improvement rates: summer declined by 67.4% (39.06 → 12.74 $\mu g\ m^{-3}$), while winter declined by only 45.7% and effectively plateaued between 2020 (60.95 $\mu g\ m^{-3}$) and 2025 (61.92 $\mu g\ m^{-3}$). The winter stagnation is attributable to the persistent meteorological bottleneck of low planetary boundary layer heights, stable stratification, and frequent temperature inversions under Wuhan's winter circulation patterns(Fan Huang et al., 2014), which negate local emission reduction efforts without trans-regional coordination. The 2025 summer mean of 12.74 $\mu g\ m^{-3}$ approaches the WHO Phase I interim target (15 $\mu g\ m^{-3}$).

Table 5. $PM_{2.5}$ concentration statistics for nine datasets ($\mu g\ m^{-3}$).

Dataset	Mean	Min (map)	Max (map)
2015 Annual	69.28	60.23	78.02
2015 Summer	39.06	32.47	47.04
2015 Winter	114	97.91	133.18
2020 Annual	40.89	31.95	46.37
2020 Summer	20.88	16.55	26.91
2020 Winter	60.95	39.36	70.25
2025 Annual	36.39	31.1	41.64
2025 Summer	12.74	6.46	16.73
2025 Winter	61.92	32	88.21

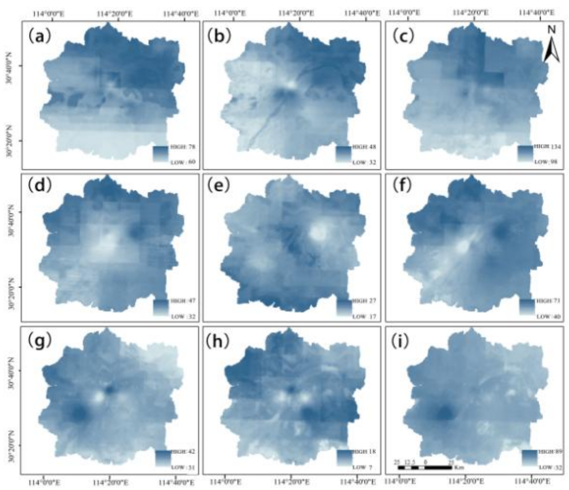

Figure 4. 250 m resolution $PM_{2.5}$ concentration distributions across nine year–season composites (2015–2025). Panels (a–c): 2015 annual, summer, and winter means; (d–f): 2020 annual, summer, and winter means; (g–i): 2025 annual, summer, and winter means. Colour scale represents $PM_{2.5}$ concentration in $\mu g\ m^{-3}$.

4.3 Urban Heat Environment Patterns (2015–2025)

Annual mean LST remained broadly stable over the decade, declining marginally from 22.10°C (2015) to 21.42°C (2025; −0.68°C; Table 6). The spatial pattern consistently reflected the urban surface energy balance — high-LST hotspots corresponded to impervious-surface-dense industrial zones (Qingshan steel and chemical complex), commercial cores, and major traffic corridors; low-LST cold islands coincided with large water bodies (East Lake, South Lake, Yangtze–Han confluence) and vegetated parks (Figure 5).

Summer and winter LST exhibited markedly divergent decadal trajectories that contrast with the stable annual mean. Summer mean LST increased monotonically by +1.39°C across the study period (31.02 → 31.96 → 32.41°C), while the summer maximum reached 40.27°C in 2020 before moderating to 38.75°C in 2025, suggesting that peak heat exposure may have partially decoupled from mean LST trends. This summer warming trend ran counter to the concurrent improvement in summer $PM_{2.5}$ (40.07 → 12.74 μg m^{-3}, −67.4%), constituting what we term the 'cleaner but hotter' paradox — the aerosol radiative brightening mechanism underpinning this divergence is discussed in Section 4.4.

Winter LST followed a non-monotonic trajectory (11.18 → 10.81 → 11.93°C), declining between 2015 and 2020 before recovering substantially by 2025. The 2015–2020 cooling is consistent with reduced solid-fuel combustion (coal-to-gas conversion suppressing low-level anthropogenic heat release) and changes in Wuhan's winter cloud cover and precipitation climatology. The 2020–2025 rebound (+1.12°C) is a noteworthy reversal that coincides with post-pandemic economic recovery and intensified winter heating demand; disentangling the relative contributions of these factors requires meteorological detrending beyond the scope of the present analysis. Consequently, the seasonal temperature range — defined as the difference between summer and winter means — expanded from 19.84°C (2015) to 20.48°C (2025), a more modest widening than a linear extrapolation from the 2015–2020 trend would suggest.

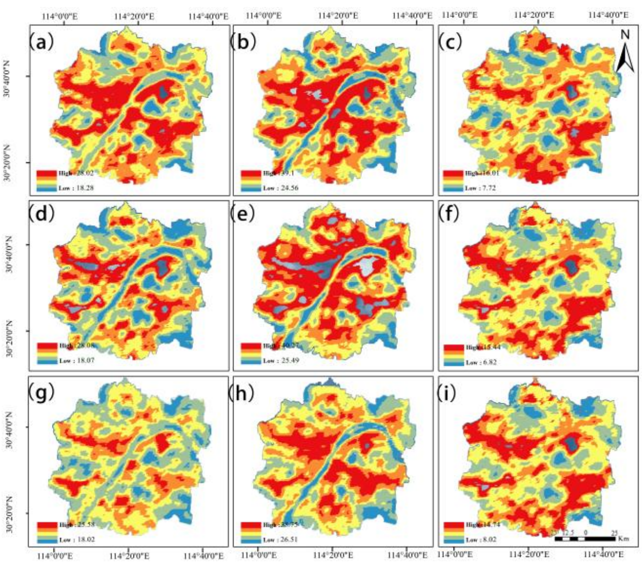

Figure 5. 250 m resolution land surface temperature (LST) spatial distribution maps across nine year–season composites (2015–2025). Panels (a–c): 2015 annual, summer, and winter means; (d–f): 2020 annual, summer, and winter means; (g–i): 2025 annual, summer, and winter means. Colour scale represents LST in degrees Celsius (°C).

Table 6. LST statistics of nine datasets (°C).

Dataset	Mean LST	Max	Min
2015 Annual	22.1	28.02	18.28
2015 Summer	31.02	39.1	24.56
2015 Winter	11.18	16.01	7.72
2020 Annual	22.09	28.08	18.07
2020 Summer	31.96	40.27	25.49
2020 Winter	10.81	15.44	6.82
2025 Annual	21.42	25.58	18.02
2025 Summer	32.41	38.75	26.51
2025 Winter	11.93	14.74	8.02

4.4 $PM_{2.5}$–LST Coupling Dynamics: Sign Reversal and Threshold Effects

Pearson correlation analysis between $PM_{2.5}$ (PM_final_250m) and downscaled LST (LST_pred_250m) at 250 m and 1 km resolution reveals a systematic, decadal evolution of the coupling structure across all nine composites (Table 7; Figure 6). Correlation magnitudes ranged from $|r| = 0.013$ to 0.335 at 250 m. Notably, three composites exhibit opposite signs at the two scales — 2015 summer (250 m: +0.013, 1 km: −0.116), 2015 annual (250 m: +0.118, 1 km: −0.018), and 2020 annual (250 m: −0.032, 1 km: +0.041) — providing direct evidence of scale-dependent mechanism divergence; the remaining six composites show sign agreement across scales in Table7 .

The dominant pattern is a progressive shift toward positive coupling, most pronounced in winter and the annual composite by 2025. In 2015 summer, the 250 m correlation was statistically significant but negligible in magnitude ($r = +0.013$, $p < 0.01$), while the 1 km scale remained negative ($r = −0.116$, $p < 0.001$) — indicating that at the coarser scale, aerosol radiative cooling was still suppressing LST in higher-$PM_{2.5}$ zones under the high-pollution conditions of 2015 (summer mean: 39.06 μg m^{-3}). By 2020, both scales showed positive summer coupling (250 m: $r = +0.064$; 1 km: $r = +0.173$), coinciding with summer $PM_{2.5}$ declining to 20.88 μg m^{-3} — a level at which aerosol radiative masking is substantially attenuated and impervious-surface co-driving begins to dominate. By 2025, the annual composite reached the strongest observed coupling (250 m: $r = +0.335$; 1 km: $r = +0.289$, both $p < 0.001$), confirming that

https://doi.org/10.5194/isprs-archives-XLIX-B3-2026-719-2026 |

urban morphology co-driving has become the structurally dominant mechanism as $PM_{2.5}$ has declined to near-compliance levels.

Winter coupling showed the most dramatic strengthening: from r = −0.047 (250 m) and r = −0.116 (1 km) in 2015, to r = +0.295 (250 m) and r = +0.268 (1 km) in 2025 — both scales positive and significant, reflecting the growing co-location of anthropogenic heat and residual $PM_{2.5}$ in dense built-up zones under winter heating demand. The 2020 annual composite (250 m: r = −0.032; 1 km: r = +0.041) represents a near-decoupled state, plausibly reflecting the disruption of normal spatial co-variation patterns by COVID-19 lockdown-induced emission suppression in 2020.

A consistent MAUP effect is evident: 1 km correlations are generally of larger magnitude than their 250 m counterparts (e.g., 2020 summer: r_{1km} = +0.173 vs. r_{250m} = +0.064; 2025 summer: r_{1km} = +0.285 vs. r_{250m} = +0.140), as spatial aggregation suppresses fine-scale heterogeneity and amplifies the regional co-driving signal. The 250 m product is nonetheless irreplaceable for neighbourhood-scale differentiation of coupling regimes.

Concentration-stratified analysis (five equal-frequency quantile bins per dataset, n ≈ 53,000 per bin) reveals that the Q5 (highest-concentration) stratum consistently produces the strongest positive coupling across all three years and seasons (Figure 7). In 2020 summer, Q5 (mean $PM_{2.5}$ = 22.9 μg m^{-3}) yields r = +0.44, the maximum bin-level signal in the summer season. The 2025 annual Q5 bin (mean $PM_{2.5}$ = 39.3 μg m^{-3}) reaches r = +0.51 — the strongest annual coupling observed — confirming that morphologically dense urban cores, where impervious surfaces simultaneously sustain elevated LST and restrict $PM_{2.5}$ dispersion, are the primary locus of positive coupling. In 2015 summer, despite the weak global r = +0.013, Q1 (lowest-$PM_{2.5}$ stratum, mean = 34.4 μg m^{-3}) already exhibits r = +0.31, indicating that the morphology co-driving pathway was already active in low-concentration peri-urban and greenspace zones even under 2015's high-pollution background.

4.5 Driving Mechanism Analysis: Feature Importance Evolution

RF feature importance scores (Figure 8) reveal three consistent patterns across the nine datasets. First, spatial coordinates (Latitude, Longitude) dominated in the majority of composites — particularly 2015 winter (Latitude ≈ 0.62) and 2015 annual (≈0.61) — confirming the primacy of spatial non-stationarity and a persistent north–south $PM_{2.5}$ gradient as the overriding explanatory dimension. Second, meteorological drivers (RH, BLP, ws, ws_u) exhibited strong seasonal modulation: RH ranked first in several summer composites (2015 summer: RH ≈ 0.31; 2020 annual: ≈0.37), reflecting hygroscopic growth of aerosols and dispersion enhancement by wind; BLP rose in winter rankings, consistent with its role as the primary dispersion-limiting factor under stable stratification. Third, AOD importance declined over the three epochs (from prominent in 2015 to outside the top-5 in most 2020 and 2025 datasets), while nighttime light (NL_MEAN) and population density (POP_MEAN) rose — particularly in 2025 annual (NL_MEAN ranked 3rd, ≈0.12). This shift mirrors the structural transition from industrial source-dominated to anthropogenic-activity-dominated $PM_{2.5}$, consistent with the spatial pattern evolution documented in Section 4.2 and the coupling mechanism transition in Section 4.4.

Table 7. Dual-scale LST–$PM_{2.5}$ Pearson correlation coefficients (nine datasets).Dual-scale LST–$PM_{2.5}$ Pearson correlation coefficients. (a) Bar chart comparison of 250 m resolution vs. 1 km resolution correlations across nine datasets. (b) Line plot showing interannual evolution by season.

Year	Season	R 250 m	Significance 250	R 1km	Significance 1km
2015	summer	0.0125	**	-0.1155	***
2015	winter	-0.047	***	-0.1158	***
2015	annual	0.1175	***	-0.0179	ns
2020	summer	0.0641	***	0.1733	***
2020	winter	0.1175	***	0.2404	***
2020	annual	-0.0316	***	0.0413	*
2025	summer	0.1403	***	0.2854	***
2025	winter	0.2949	***	0.2676	***
2025	annual	0.335	***	0.2891	***

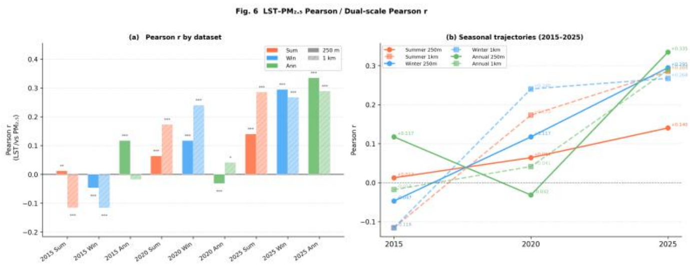

Figure 6. Dual-scale LST–$PM_{2.5}$ Pearson correlation coefficients.
Note. (a) Bar chart comparison of 250 m vs. 1 km correlations across nine datasets. (b) Line plot showing interannual evolution by season.

5. Conclusions

1) Methodological robustness: RF outperformed XGBoost and LightGBM on all nine datasets (R^2: 0.531–0.936; |Bias| ≤ 0.10 μg m^{-3}). IDW correction reduced RMSE by an average of ~35% (best case: 64%, 2020 summer). LOO-CV confirmed that the performance gains are spatially independent and not artefacts of spatial autocorrelation. $PM_{2.5}$ improvement with a winter bottleneck: Annual mean $PM_{2.5}$ declined 47.5% over the decade (69.28 → 36.39 μg m^{-3}). Summer approached the WHO Phase I interim target (12.74 μg m^{-3} in 2025).
2) Winter concentrations plateaued between 2020 and 2025 (~61 μg m^{-3}), signalling a meteorological dispersion bottleneck

that local emission control alone cannot overcome — requiring trans-regional coordination.

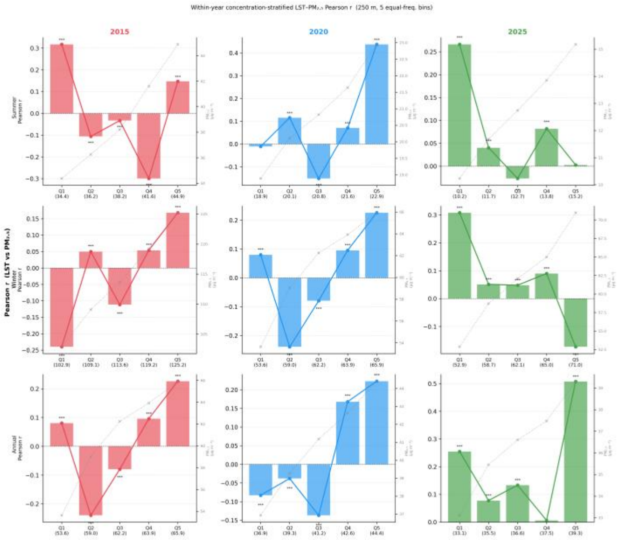

Figure7. Concentration-stratified LST–$PM_{2.5}$ correlation (250 m, 5 quantile bins). Rows: summer, winter, annual. Columns: 2015, 2020, 2025. Colours: red = 2015, blue = 2020, green = 2025.

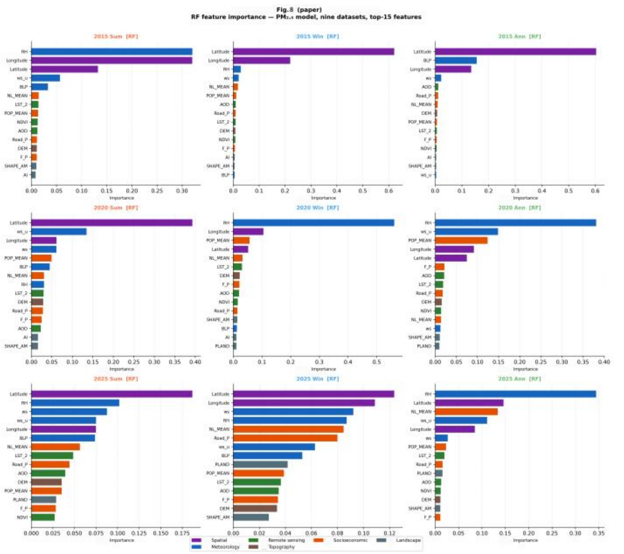

Figure 8. RF feature importance for all nine datasets (top-15 features per dataset). Colour-coded by feature category: meteorology (blue), remote sensing (green), socioeconomic (orange), landscape (grey), spatial (purple).

3) Cleaner but hotter' paradox: Summer LST increased +1.39°C (2015–2025) while summer $PM_{2.5}$ declined by 67.4%, consistent with an aerosol radiative brightening feedback: reduced aerosol concentrations increase surface-reaching shortwave radiation, amplifying urban surface heating in the absence of compensating land-cover change.
4) Progressive coupling reversal: The LST–$PM_{2.5}$ spatial correlation at 250 m resolution evolved from near-zero in 2015 summer ($r = +0.013$) and weakly negative in 2015 winter ($r = -0.047$) to strongly positive across all composites by 2025 (annual: $r = +0.335$; winter: $r = +0.295$), reflecting a decade-scale mechanistic transition from aerosol radiative cooling to urban morphology co-driving. Concentration-stratified analysis demonstrates that the Q5 (highest-$PM_{2.5}$) stratum consistently drives the strongest positive coupling, reaching $r = +0.51$ in the 2025 annual composite — a quantitative reference directly applicable to co-management planning.
5) Scalable framework: The three-stage approach is transferable to other Chinese megacities with comparable monitoring infrastructure. Future extensions should integrate causal inference methods (e.g., causal forest) to move beyond correlation and quantify the direct aerosol radiative forcing contribution to LST change, and fuse emission inventory data to disentangle the relative contributions of source category transitions.References

6. Acknowledgements

This work was supported by the National Natural Science Foundation of China (No.: 52078389, 51878515) .

7. Reference

Akbari, H., Pomerantz, M., Taha, H., 2001. Cool Surfaces and Shade Trees to Reduce Energy Use and Improve Air Quality in Urban Areas. *Solar Energy*, Urban Environment, vol. 70 (3): 295–310. https://doi.org/10.1016/S0038-092X(00)00089-X.

Cao, W., Zhou, W., Yu, W., Wu, T., 2024.Combined Effects of Urban Forests on Land Surface Temperature and PM2.5 Pollution in the Winter and Summer. *Sustainable Cities and Society,* 104 (May 2024): 105309. https://doi.org/10.1016/j.scs.2024.105309.

Chen, J., Zhan, W., Jin, S., Han, W., Du, P., Xia, J., Lai, J., et al., 2021. Separate and Combined Impacts of Building and Tree on Urban Thermal Environment from Two- and Three-Dimensional Perspectives. *Building and Environment,* 194 (May 2021): 107650. https://doi.org/10.1016/j.buildenv.2021.107650.

Chen, Xin, and Fang Wei. 2025.Chen, X., Wei, F., 2025.Morphology on Land Surface Temperature and PM2.5 Concentration across Fine-Scale Urban Blocks in Hangzhou, China. *Building and Environment,* 278 (June 2025): 112979. https://doi.org/10.1016/j.buildenv.2025.112979.

Chen, Y., Zhang, R., Alekouei, S.A., Amani-Beni, M., 2024. Nonlinear Impacts of Landscape and Climatological Interactions on Urban Thermal Environment during a Hot and Rainy Summer. *Ecological Indicators,* 166 (September 2024): 112551. https://doi.org/10.1016/j.ecolind.2024.112551.

Cohen, A.J., Brauer, M., Burnett, R., Anderson, H.R., Frostad, J., Estep, K., Balakrishnan, K., et al., 2017. Estimates and 25-Year Trends of the Global Burden of Disease Attributable to Ambient Air Pollution: An Analysis of Data from the Global Burden of Diseases Study 2015. *The, Lancet,* 389 (10082): 1907–1918.https://doi.org/10.1016/S0140-6736(17)30505-6.

Di, Q., Amini, H., Shi, L., Kloog, I., Silvern, R., Kelly, J., Sabath, M.B., et al., 2019. An Ensemble-Based Model of PM2.5 Concentration across the Contiguous United States with High Spatiotemporal Resolution. *Environment International,* 130 (September 2019): 104909. https://doi.org/10.1016/j.envint.2019.104909.

Geng, Guannan, Qingyang Xiao, Shigan Liu, Xiaodong Liu, Giridharan, R., Emmanuel, R., 2018.Tracking Air Pollution in China: Near Real-Time PM2.5 Retrievals from Multisource

Data Fusion. *Environmental Science & Technology,* 55 (17): 12106–12115. https://doi.org/10.1021/acs.est.1c01863.

Giridharan, Renganathan, and Rohinton Emmanuel. 2018. The Impact of Urban Compactness, Comfort Strategies and Energy Consumption on Tropical Urban Heat Island Intensity: A Review. *Sustainable Cities and Society,* 40 (July 2018): 677–687. https://doi.org/10.1016/j.scs.2018.01.024.

Guo, G., Wu, Z., Xiao, R., Chen, Y., Liu, X., Zhang, X., 2015.Impacts of Urban Biophysical Composition on Land Surface Temperature in Urban Heat Island Clusters. *Landscape and Urban Planning,* 135 (March 2015): 1–10. https://doi.org/10.1016/j.landurbplan.2014.11.007.

Huang, F., Zhan, W., Duan, S.-B., Ju, W., Quan, J., 2014. A Generic Framework for Modeling Diurnal Land Surface Temperatures with Remotely Sensed Thermal Observations under Clear Sky. *Remote Sensing of Environment,* 150 (July 2014): 140–151. https://doi.org/10.1016/j.rse.2014.04.022.

Huang, X., Li, J., Yang, J., Zhang, Z., Li, D., Liu, X., 2021. 30 m Global Impervious Surface Area Dynamics and Urban Expansion Pattern Observed by Landsat Satellites: From 1972 to 2019. *Science China Earth Sciences,* 64 (11): 1922–1933. https://doi.org/10.1007/s11430-020-9797-9.

Huang, X., Song, Y., Yang, J., Wang, W., Ren, H., Dong, M., Feng, Y., Yin, H., Li, J., 2022. Toward Accurate Mapping of 30-m Time-Series Global Impervious Surface Area (GISA). *International Journal of Applied Earth Observation and Geoinformation,* 109 (May 2022): 102787. https://doi.org/10.1016/j.jag.2022.102787.

Kouis, P., Kakkoura, M., Ziogas, K., Paschalidou, A.K., Papatheodorou, S.I., 2019. The Effect of Ambient Air Temperature on Cardiovascular and Respiratory Mortality in Thessaloniki, Greece. *Science of The Total Environment,* 647 (January 2019): 1351–1358. https://doi.org/10.1016/j.scitotenv.2018.08.106.

Li, Y., Wanlu O., Shi Y., Zheng T., and Chao Ren., 2023. Microclimate and Its Influencing Factors in Residential Public Spaces during Heat Waves: An Empirical Study in Hong Kong. *Building and Environment,* 236 (May 2023): 110225. https://doi.org/10.1016/j.buildenv.2023.110225.

Lin, X., Dong, Y., Teng, Z., Meng, Z., Zhang, F., Hu, X., Wang, Z., 2025. Spatiotemporal Correlations of PM2.5 and O3 Variations: A Street-Scale Perspective on Synergistic Regulation. *Science of The Total Environment,* 965 (February 2025): 178578. https://doi.org/10.1016/j.scitotenv.2025.178578.

Ngarambe, J., Joen, S.J., Han, C.-H., Yun, G.Y., 2021. Exploring the Relationship between Particulate Matter, CO, SO2, NO2, O3 and Urban Heat Island in Seoul, Korea. *Journal of Hazardous Materials,* 403 (February 2021): 123615. https://doi.org/10.1016/j.jhazmat.2020.123615.

Oke, T. R. 1982. The Energetic Basis of the Urban Heat Island. *Quarterly Journal of the Royal, Meteorological Society,* 108 (455): 1–24. https://doi.org/10.1002/qj.49710845502.

Peng C., Chunyu Dai, Jun Z., and Ting i. 2022. Assessing the Effects of Urban Morphology Parameters on PM2.5 Distribution in Northeast China Based on Gradient Boosted Regression Trees Method. *Sustainability*, ahead of print, 24 February 2022. https://doi.org/10.3390/su14052618.

Shao, L., Liao, W., Li, P., Luo, M., Xiong, X., Liu, X., 2023. Drivers of Global Surface Urban Heat Islands: Surface Property, Climate Background, and 2D/3D Urban Morphologies. *Building and Environment,* 242 (August 2023): 110581. https://doi.org/10.1016/j.buildenv.2023.110581.

Wang, X., Rahman, M.A., Mokroš, M., Rötzer, T., Pattnaik, N., Pang, Y., Zhang, Y., Da, L., Song, K., 2023. The Influence of Vertical Canopy Structure on the Cooling and Humidifying Urban Microclimate during Hot Summer Days. *Landscape and Urban Planning,* 238 (October 2023): 104841. https://doi.org/10.1016/j.landurbplan.2023.104841.

Wang, Z., Fan, C., Zhao, Q., Myint, S.W., 2020. 17 A Geographically Weighted Regression Approach to Understanding Urbanization Impacts on Urban Warming and Cooling: A Case Study of Las Vegas. *Remote Sensing,* 12 (2): 2. https://doi.org/10.3390/rs12020222.

Wong, N.H., Tan, C.L., Kolokotsa, D.D., Takebayashi, H., 2021. Greenery as a Mitigation and Adaptation Strategy to Urban Heat. *Nature Reviews Earth & Environment,* 2 (3): 166–181. https://doi.org/10.1038/s43017-020-00129-5.

Wu, H., Yang C., Tijian W., Jiawei Y., Tingting Y., Yawei Q., Shuqi Y., et al., 2024. How Does PM2.5 Impact the Urban Vertical Temperature Structure? A Case Study in Nanjing. *Aerosol and Air Quality Research*, ahead of print, 2024. https://doi.org/10.4209/aaqr.230214.

Xiao, Q., Geng, G., Liu, S., Liu, J., Meng, X., Zhang, Q., 2022.Spatiotemporal Continuous Estimates of Daily 1 Km $PM_{2.5}$ from 2000 to Present under the Tracking Air Pollution in China (TAP) Framework. *Atmospheric Chemistry and Physics,* 22 (19): 13229–13242. https://doi.org/10.5194/acp-22-13229-2022.